Transport properties of Co₂HfSn Heusler alloy obtained by rapid solidification and sintering

Alessandro Difalco [a], Ignatio G. Winning [a], Mauro Palumbo [a], Marcello Baricco [a], Alberto Castellero [a,b,*], Eric Alleno [c]

[a] *Dipartimento di Chimica, NIS, INSTM, Università di Torino, Via P. Giuria 7, Torino, Italy*
[b] *CNR-ICMATE, Corso Stati Uniti 4, Padova, Italy*
[c] *Univ Paris Est Creteil, CNRS, ICMPE, UMR, 7182, 2-8, Rue H. Dunant, F-94320, Thiais, France*

ARTICLE INFO

ABSTRACT

Co-based Heusler alloys are attracting considerable interest as they were found to be suitable for spin-injection processes, and for the generation of spin-polarized currents via spin-Seebeck effect. Co₂HfSn has been proved to be one of the most promising candidates for this application, since it combines remarkable half-metallic properties, compositional and doping versatility, ease of preparation, high Curie temperature, and sufficiently high Seebeck coefficient. In this work, the Co₂HfSn Heusler compound was synthesized by rapid solidification (melt-spinning) followed by spark plasma sintering. Electron backscattered diffraction (EBSD) analysis was performed, providing useful information on the microstructure and grain size distribution which result from such processing route. An average grain size of approximately 5 μm was observed. The electronic and thermal transport properties were then measured, and the thermoelectric figure of merit zT was experimentally estimated for the first time, having a maximum value of 0.040 at 800 K. The electrical conductivity and the charge carrier concentration were measured down to 2 K to collect evidence on the shape of the electronic density of states in proximity of the Fermi level at temperatures close to absolute zero. A change of regime of the electrical conductivity at low temperatures was found and explained in terms of a modification of the electron scattering mechanisms, due to a crossover from a half-metallic to a conductive state at 75 K. Finally, the transport, elastic and vibrational properties were calculated using Density Functional Theory (DFT). Properties such as the Seebeck coefficient and the electronic thermal conductivity were evaluated using DFT-calculated electronic bands within the framework of Boltzmann transport theory. Vibrational properties, such as phonon band structure, density of states and heat capacity were computed in the harmonic approximation, using DFT to calculate the force constants matrix. Results from calculations of the elastic moduli enabled us to apply Slack's model for the estimation the lattice thermal conductivity. By combining experimental measurements with DFT calculations, we obtained consistent results that offer a deeper understanding of the properties of this compound at both low and high temperatures.

1. Introduction

Heusler alloys are ternary intermetallic compounds of X₂YZ stoichiometry (where X and Y are late and early transition metals, respectively, Z is a p-group element) which crystallize in the L2₁ structure [1, 2]. In particular, this structure consists of four inter-penetrating fcc sublattices arranged in highly ordered configuration. Fe-based Heusler alloys, such as Fe₂VAl, are renowned thermoelectric materials. They exhibit high Seebeck coefficients and thermoelectric figures of merit,

thus historically garnering significant attention [1–6]. Co-based Heusler compounds, in contrast, are not typically semiconductive. As a result, their thermoelectric properties often lag behind their Fe-based counterparts [7–10]. However, their unique electronic structure has recently generated great interest, especially in areas such as spintronics and spin-injection technologies [11–13]. A large number of Co-based Heusler compounds were indeed found to be half-metallic ferromagnets, such as Co₂CrAl [14], Co₂MnSi [15], Co₂FeSi [16], Co₂V(Al,Ga) [17,18], Co₂FeAl₀.₅Si₀.₅ [19], Co₂Ti(Si,Ge,Sn) [10], Co₂ZrSn [20,21],

and Co$_2$HfSn [21,22]. This makes them subjects of increasing research attention for potential spintronic devices, operating close to room temperature. Despite their importance for the development of spin-voltage generators [23,24], characterizations of properties for such alloys are relatively sparse in literature. This is surprising, given the efficacy of the spin-Seebeck effect in generating and transmitting spin-polarized currents over considerable distances [25].

In a previous work [26], we reported the Seebeck coefficient (*S*), electrical conductivity (*σ*) and power factor (PF) of Co$_2$HfSn measured from room temperature up to 773 K. A 7 % wt. of Co$_2$Hf secondary phase was present in the samples used in that study. The *S* trend was found to be peculiar: linear growth below the Curie temperature (*T*$_C$), estimated around 426 K, followed by an extended plateau above it. At room temperature, a value of *S* around −13 μV/K was found, settling then on the plateau around −38 μV/K. Additionally, the electrical conductivity was reported to decrease as a function of temperature below *T*$_C$, showing a metallic-like behavior, and to slightly increase above *T*$_C$. Half-metallicity evidence primarily stemmed from magnetization measurements and ab-initio calculations [21,22], but a peculiar trend of magnetization against temperature was reported [21]. In particular, a crossover from a high temperature Stoner regime (where the magnetization *M* is linearly proportional to *T*^{2}) to a low temperature Bloch behavior (where *M* ∝ *T*$^{3/2}$) was observed around 30 K. This was attributed to a change in the spin-flip mechanism due to the possible presence of a half-metallic band-gap at low temperatures, as already observed in other Heusler compounds [27]. Ab-initio calculations have predominantly focused on transport and electronic property calculations to elucidate the half-metallic nature of this alloy [21,22,28,29].

The aim of this work is to investigate the electronic and thermal transport properties of the Co$_2$HfSn Heusler alloy, spotlighting its potential for spintronic and spin-injection applications. The rapid solidification process notably expands the stability domain of the Heusler phase, paving the way for consistent single-phase sample preparation and untainted compound characterization. In fact, the presence of secondary phases is known to be a major preparation issue with Heusler alloys [30]. The fast quenching rate also favors microstructure refinement, enhancing the thermoelectric figure of merit. Quantitative information on such microstructure has been obtained from electron backscattered diffraction (EBSD) analysis, as well as SEM-EDS. The thermoelectric properties were measured in Co$_2$HfSn to assess its potential as a thermoelectric material and to better establish its electronic ground state and lattice dynamics. The electrical conductivity at low temperature has shown a peculiar behavior, consisting in a low-*T* *σ*/*T*^{2} regime, followed by a *σ*/*T*$^{1.40}$ above 75 K. This has been explained, similarly to other Heusler compounds [27,31], by considering a change in the electronic scattering mechanisms induced by a crossover from a half-metallic to an itinerant ferromagnetic state. The figure of merit *zT* of Co$_2$HfSn was experimentally estimated here for the first time. The electronic transport properties, phonon density of states, and phonon band structure in the harmonic approximation were also evaluated by ab-initio calculations in order to perform a comparison between the experimental results and the expected value for the defect-free system. Additionally, the elastic moduli, Debye temperature and Grüneisen parameter were calculated from Density Functional Theory (DFT) calculations, employing them within Slack's model to gauge the lattice thermal conductivity. Experimental and calculated properties show a good agreement.

2. Materials and methods

The elemental metals (Co 99.97 %, Hf 99.7 %, Sn 99.97 % purity) were weighted in appropriate stoichiometric quantities and melted in an Edmund Buhler GmbH (Bodelshausen, Germany) arc-furnace. The sample was melted several times to ensure homogeneity. The alloy was then re-melted in a boron nitride crucible and injected onto a rotary copper wheel (20 m/s speed) using an Edmund Buhler GmbH melt-

spinning apparatus. The rapidly solidified material was hand-grinded into powder and subsequently sintered by spark plasma sintering (SPS) with a Fuji 515 S equipment. Graphite molds lined with graphite paper were used to obtain pellets 8–10 mm in diameter and approximately 2.5 mm thick. After several trials, good sintering conditions were determined to be 1373 K for the temperature, 66 MPa for the pressure, and 1 min for the dwell time, reaching a relative density of 95 % with respect to the theoretical one.

The structural properties of the samples were analyzed by X-rays diffraction (XRD) in Bragg-Brentano geometry using a PANalytical X'Pert Pro diffractometer. The XRD patterns were refined with the Rietveld method using MAUD software [32]. Microstructural characterizations have been obtained by Scanning Electron Microscopy (SEM) using a TESCAN Vega 4 equipped with an Oxford Instruments energy dispersion spectroscopy (EDS) Ultim Max 40 probe. The electron back-scattered diffraction analysis was performed on a flat sample polished down to 40 nm with a TESCAN S9000G FESEM equipped with an Oxford Instruments Symmetry S3 EBSD probe.

The electrical resistivity (four-probes, Van Der Pauw geometry) and Seebeck coefficient were measured on a bar-shaped sample obtained from a the sintered pellet, using a custom apparatus described in detail in Ref. [33], with a thermal gradient of ΔT ∼ 2 K. A 8 mm wide, 2 mm thick cylindrical disk was used for the measurement of the thermal diffusivity between 300 K and 800 K on a Netzsch LFA 427 laser flash, whereas the specific heat capacity (*C*$_p$) was obtained on a PerkinElmer DSC 8000 calorimeter. The Hall effect and the electrical resistivity below room temperature were collected with a Quantum Design physical properties measurement system, PPMS (DC mode, Van Der Pauw geometry), from 2 K to 300 K, and, in the latter case, by varying the magnetic field between 7 and -7 T.

Ab-initio calculations were performed using Vienna Ab-initio Simulation Package (VASP) [34], using the projector augmented plane (PAW) method [35]. For magnetic effects, spin-polarized collinear magnetic configurations were considered and spin flips were allowed. For evaluating the transport properties and elastic moduli, the same computational settings already described in Ref. [21] were used. Transport properties were post-processed using the BoltTraP2 code, based on the Boltzman transport theory [36]. In order to obtain phonon properties, the Co, Hf_pv, Sn_d pseudopotentials from the standard VASP library [37] and Perdew-Burke-Ernzerhof (PBE) [38] functional were used in a 2 × 2 × 2 supercell (128 atoms in total) sampled with a 7 × 7 × 7 Monkhorst-pack [39] k-points grid. The energy cutoff was set at 500 eV. These computational settings ensure that no artificial imaginaries frequencies are found in the phonon bands. The force constants matrix and the post-processing data treatment for the calculations of the phonon band structure, phonon density of states (p-DOS) and thermal properties in the harmonic approximation were performed with the Phonopy code [40].

3. Results and discussion

3.1. Structural and microstructural characterization

Fig. 1(a) shows the experimental XRD pattern (open circles) of a pulverized sample taken from a sintered pellet. This is juxtaposed with the fitted pattern (red line) obtained through Rietveld refinement and the difference between experimental and calculated patterns (blue line). The XRD analysis reveals that the sample is monophasic, with only the L2$_1$ Co$_2$HfSn Heusler phase detected. On the other hand, SEM analysis, Fig. 1(b), shows small impurities of C15-type Co$_2$Hf Laves phase. These impurities are present in such small quantities that they fall below the detection threshold of the XRD technique. The good quality of the fit confirm that this compound effectively crystalizes in the ordered L2$_1$ structure. The lattice parameter (*a*) of the Co$_2$HfSn compound was determined to be 6.2211 Å, slightly different from the value of 6.2157 Å, previously reported for a non-monophasic sample [26]. Other
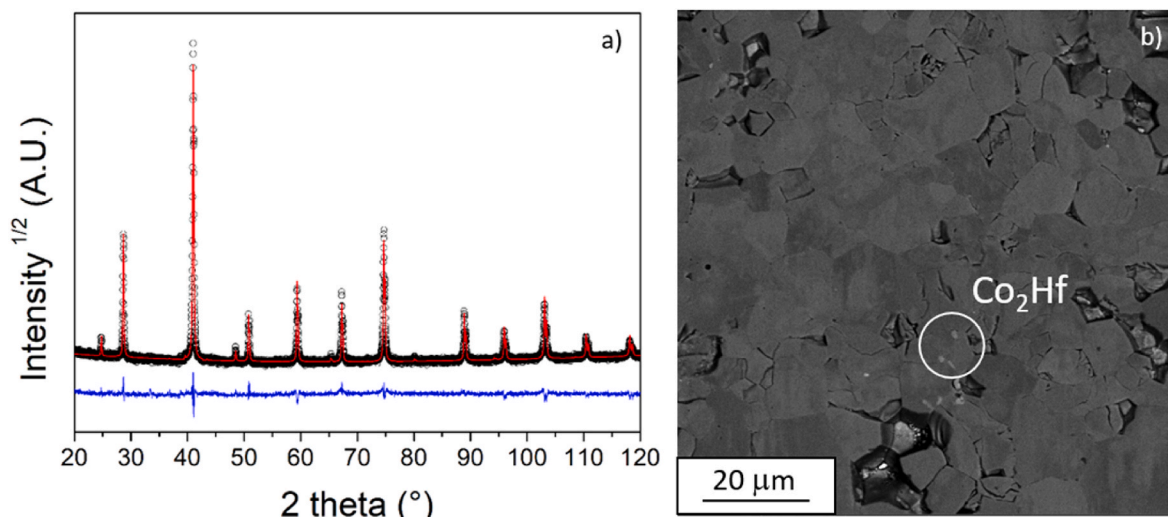
Fig. 1. (a) XRD analysis of the sintered Co$_2$HfSn sample (open circles: experimental; red line: calculated; blue line: difference between experimental and calculated); (b) SEM image (backscattered electrons) of the sintered sample: since the sample was polished down to a 40 nm roughness, it is possible to distinguish between grains of the same phase based on their different orientation (which correspond to different grey tones).

experimental lattice parameter values reported in the literature vary between 6.218 Å [41] and 6.236 Å [22]. This variation underscores the significant influence that different processing methods exerts on the structural properties of the Heusler phase. Results of the Rietveld analysis of XRD patterns of the arc melted as-cast, annealed and melt-spun Co$_2$HfSn alloy can be found in Fig. S1 of the Supplementary Material. A weight percentage of 2 % of Co$_2$Hf secondary phase was found in the as-cast specimen, and the same quantity was detected after annealing at 1273 K for 6 days. Furthermore, after the rapid solidification process, the melt-spun material was observed to be fully monophasic. This suggests that the fast cooling rate enhances the experimentally achievable compositional range for the Heusler phase.

EDS measurements on the sintered pellet revealed atomic relative abundances (at.%) of 48 %, 25 %, 27 % of Co, Hf and Sn, respectively, suggesting the presence of a monophasic Heusler phase with the aforementioned composition in the sample. The small impurities of secondary phases displayed an atomic composition of 66 % Co, 29 % Hf, 4 % Sn, which is consistent with findings reported in the literature [26]. To gain a comprehensive understanding and obtain quantitative data on the microstructure resulting from the selected processing method, an EBSD analysis has been performed on polished sintered pellets. As it can be noticed from Fig. 2(a), the sample appears basically monophasic, as only the Heusler phase (light blue) was identified. Small grains of Co$_2$Hf (green) were also found; however, their relative abundance was estimated to be lower than 0.25 %. Therefore, the presence of this secondary phase will be deemed negligible in subsequent discussion. SEM images, Fig. 2(b), also reveals the presence of porosities of various sizes in the sample; nevertheless, a relative density of 95 % (10.8 g/cm^3) was measured compared to the theoretical value for the bulk material (11.4 g/cm^3). In Fig. 2(c), an EBSD grain orientation map is presented, where individual grains are color-coded based on their crystallographic orientation relative to a specified axis. For this representation, the map corresponds to the z-axis, aligning with the pressure direction during the SPS process. Given the random color distribution across the entire sample area, it is evident that the sintered pellet does not display any preferential grain orientation. Additionally, Fig. 2(a) and (c) further highlight that the grains are predominantly equiaxed, with a peak-distribution of the ellipsoid aspect ratio of 1.41. This suggests the presence of nearly spherical grains (for the ellipsoid aspect ratio distribution, see Fig. S2 of the Supplementary Material). EBSD analysis also allowed to determine the grain size distribution, as shown by the histogram in Fig. 2(d) together with the related fit (red line). From the

distribution, we estimated an average grain size around 5 μm, suggesting a relatively fine microstructure.

3.2. Transport properties

The electronic transport properties of Co$_2$HfSn are shown in Fig. 3. The Seebeck coefficient was measured from 300 K up to 800 K, both during heating (empty black circles connected by the back line) and cooling (empty red circles) cycles, to ensure the absence of hysteresis. In Fig. 3(a), it is possible to observe a trend that is both qualitatively and quantitatively coherent to that already reported in the literature [26]. At room temperature, the S value stands at -13 μV/K and it then exhibits a linear increase in absolute value, rising at a rate of approximately 0.20 μV/K^2 up to 426 K. Beyond this temperature, the Seebeck coefficient stabilizes, settling at a plateau value of about -41 μV/K up to 800 K. The negative value of S indicates that electrons are the dominant charge carriers.

The electrical conductivity (σ) between 300 K and 800 K is shown in Fig. 3(b), reporting both heating (empty black circles connected by the back line) and cooling cycles (empty red circles). At room temperature, σ stands at 4718 S/cm, then it decreases almost linearly at a rate of about -13.57 S cm^{-1}K^{-1}, bottoming out at 3300 S/cm. Beyond this point, σ starts to weakly rise at a rate close to 0.56 S cm^{-1}K^{-1}, reaching a value of 3496 S/cm at 800 K. For such compounds the temperature at which σ changes its slope corresponds to the Curie point, T_C, where the transition from ferromagnetic to paramagnetic behaviour occurs [10]. For this sample a T_C of 426 K is estimated from Fig. 3(b) and the value obtained corresponds to the temperature at which the Seebeck coefficient reaches the plateau, Fig. 3(a). As previously reported [26], the linear decrease of σ below T_C indicates the metallic behaviour of the alloy in the ferromagnetic state. Conversely, a weak increase of σ is observed in the paramagnetic state above T_C. As the power factor ($PF=S^2\sigma$) is largely dominated by S, similar patterns emerge in Fig. 3(a) and (c).

Fig. 3(d) delineates the trend of σ from room temperature down to 2 K. Here, a noticeable variation in the σ vs T trend is evident: from a parabolic pattern below 75 K to a nearly linear behaviour above this threshold. This peculiar behaviour, previously observed also in other Heusler compounds, was explained by the transition from a low-temperature half-metallic state to a at high-temperature conductive state [27,31]. The half-metallic state, because of the absence of a minority-spin density of states at the Fermi level, renders the spin-flip electron scattering unfeasible, leading to the observed pattern [42,43].
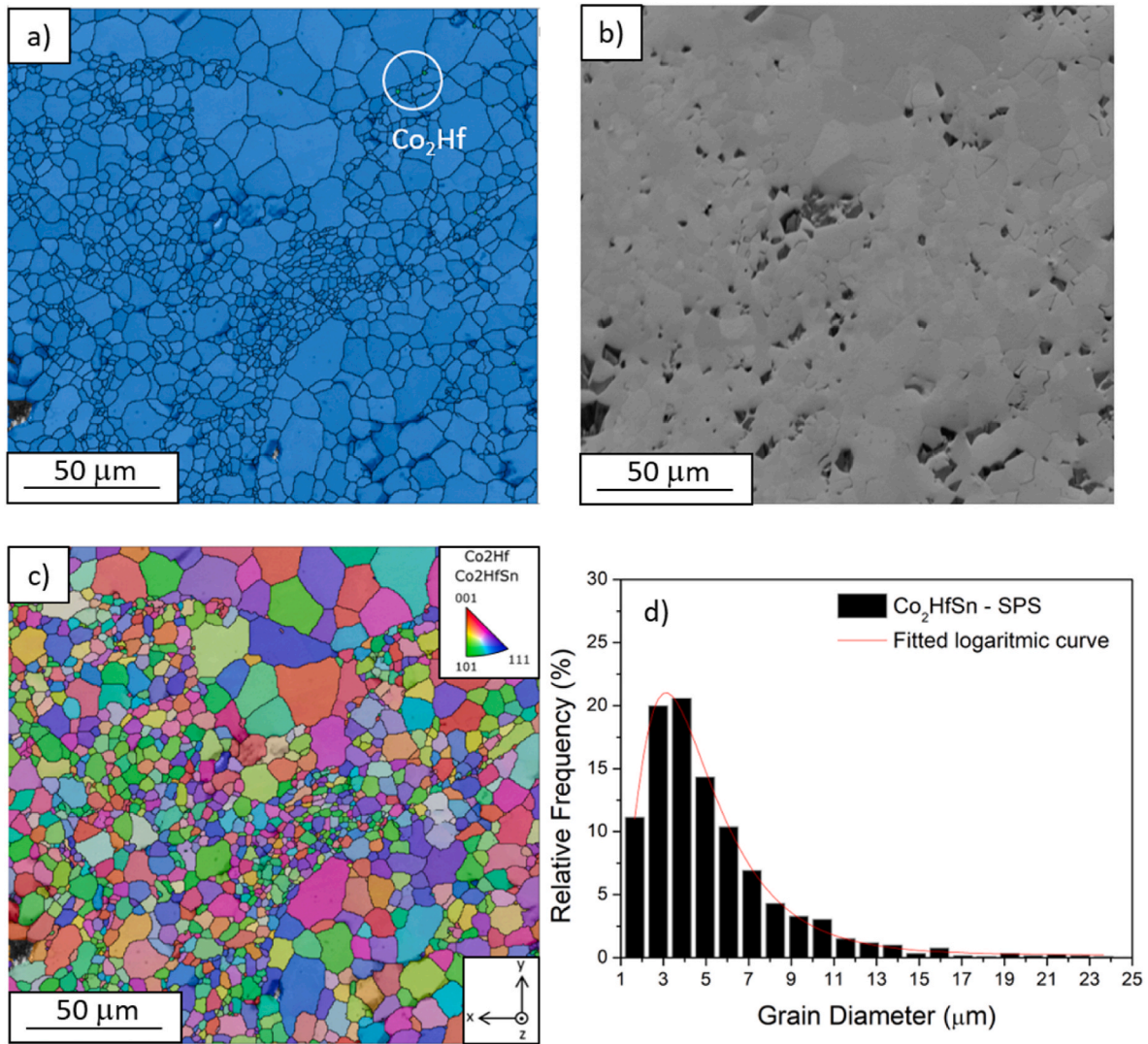
Fig. 2. FESEM micrographs of the sintered Co_2HfSn sample, obtained with different detectors: (a) EBSD map (light blue: Co_2HfSn, green: Co_2Hf); (b) backscattered electron detector; (c) EBSD grains orientation map along the z direction. (d) Grain size distribution of the Co_2HfSn Heusler phase (histogram: experimental distribution, red line: logarithmic fit).

Conversely, at elevated temperatures, multiple electronic scattering mechanisms come into play, including spin waves, phonons, and spin fluctuations. This results in a σ–dependency on T with an exponent ranging between 1 and 5/3 [27,44], consistent with the exponent value of 1.40 derived from the fit of our experimental data. It should be noted that, similarly to other half-metallic Heusler compounds [27], Co_2HfSn exhibits a regime shift in magnetization (M) analogous to σ, with a crossover temperature around 30 K [21]. As far as magnetization is concerned, this regime change is again ascribed to a transition from a low-temperature half-metallic state to a high-temperature conductive state [21,27,31,45].

The Hall resistivity and charge carrier concentration were also measured from 2 to 300 K. An anomalous contribution (see Fig. S3 of the Supplementary Material) was observed between no-field conditions and 1 T. However, at higher magnetic fields (H) only the ordinary contribution is evident, as illustrated in Fig. 4(a). Values of Hall resistivity (R_H) between 1 and 7 T are remarkably consistent, as evident when comparing the slopes of the respective lines in Fig. 4(a), all converging to a value of approximately $5.8 \cdot 10^{-10}$ m³/C. The charge carrier concentration (n) was calculated as a function of T using the R_H values, according to the relation $n = (R_H\,e)^{-1}$, where e is the electron charge, and results are shown in Fig. 4(b). Here, it is noteworthy that n remains

largely unaffected by temperature changes up to room temperature, maintaining a nearly constant value of about $1 \cdot 10^{28}$ m⁻³, a characteristic value for conductive materials.

The trends of the thermal diffusivity and thermal conductivity, k, as a function of T are reported in Fig. 5(a) and (b), respectively. The latter was obtained by multiplying the thermal diffusivity, the density and the specific heat capacity, Fig. 5(c). Both thermal diffusivity and thermal conductivity show a trend as a function of temperature that mirrors the one of σ, Fig. 3(b), with a linear decline from room temperature up to approximately T_C and followed by a linear increase after it. With this data, the electronic, k_{el} (open black squares), and lattice, k_{lat} (open red triangles), contributions to k (filled black circles) were calculated, and they are illustrated in Fig. 5(b). The Wiedemann-Franz ($k_{el} = L\sigma T$) law was employed, with $L = 1.5 + exp\left[-\frac{|S|}{116}\right]$ WΩK⁻² the Lorentz number as proposed by Snyder et al. [46] and $k_{lat} = k - k_{el}$ [47]. From Fig. 5(b), one can discern that, below approximately 700 K, the main contribution to k is given by the lattice component. However, above this temperature, the electronic component becomes increasingly dominant. The specific heat capacity (C_p) as a function of temperature, Fig. 5(c), reveals a peak with the typical lambda shape in proximity of T_C, and after the transition remains rather constant ($\sim$0.48 Jg⁻¹K⁻¹, or 200.2 JK⁻¹ per mole of formula unit). This pattern is coherent with observations for other
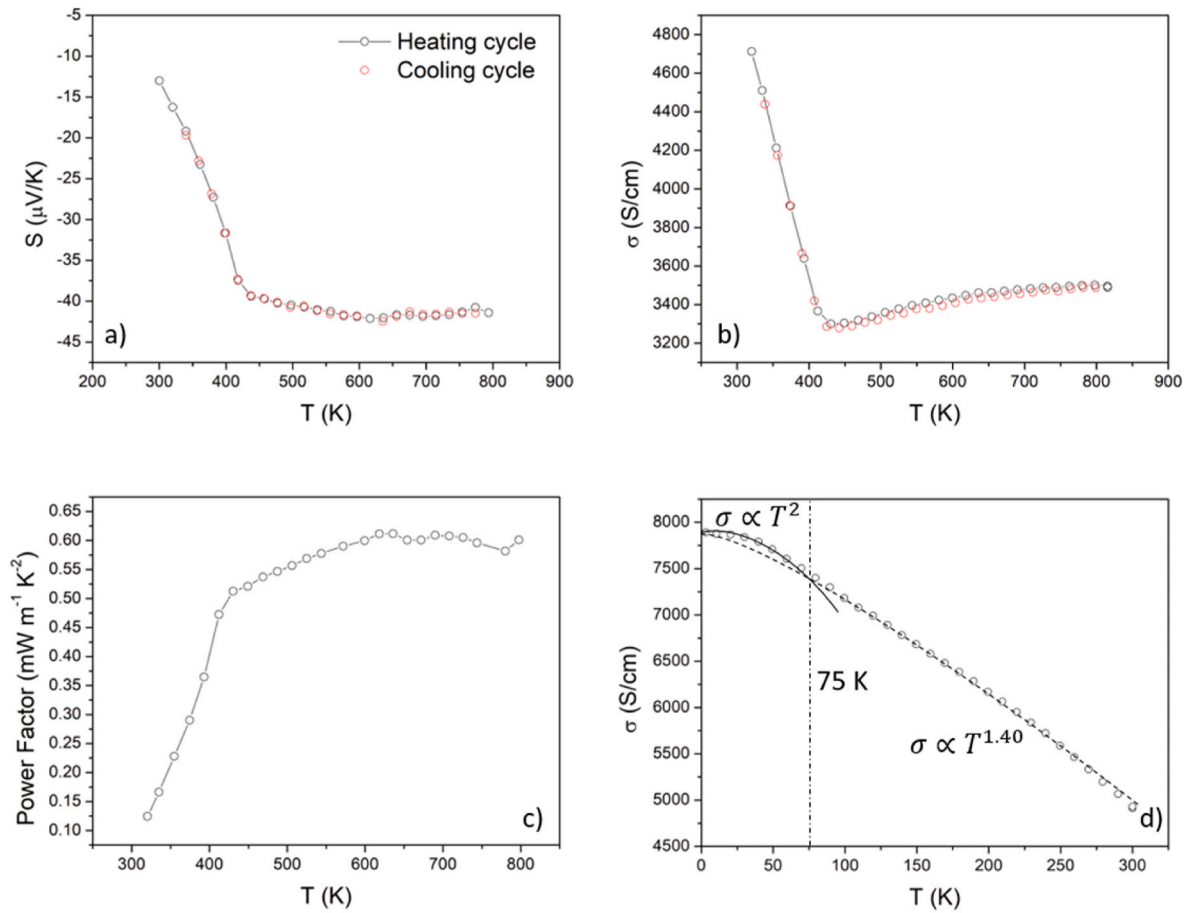
Fig. 3. Electronic transport properties of sintered Co_2HfSn. Seebeck coefficient (a), electrical conductivity (b) and power factor (c) between 300 K and 800 K (the black lines connecting the open black circles are a guide to the eye). Low temperature electrical conductivity between 2 K and 300 K (d) (open circles represent experimental values, the continuous and dashes lines are fitting curves).
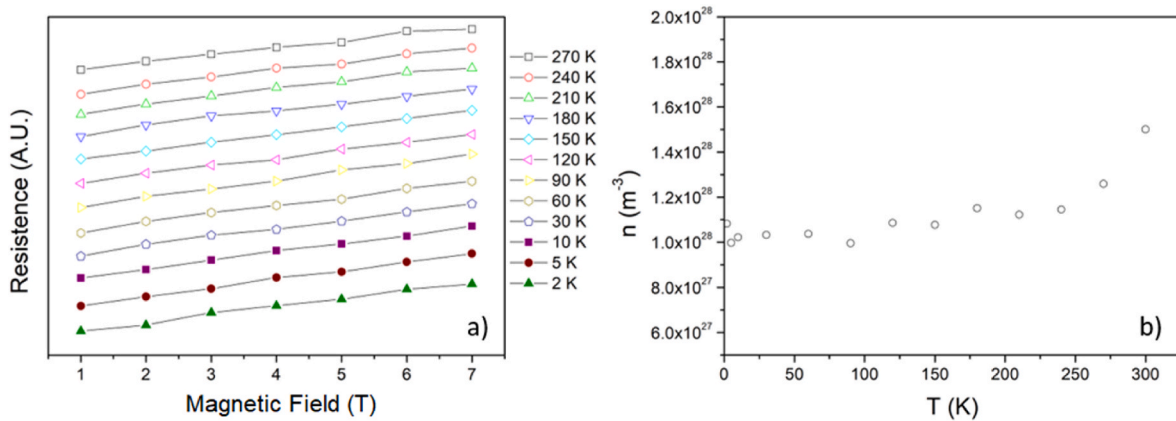

Fig. 4. (a) Hall resistivity as a function of magnetic field; (b) charge carrier concentration as a function of temperature for sintered Co_2HfSn.

similar compounds reported in the literature [48]. The kink at T_C in k_{lat} arises from an incomplete compensation of the diffusivity dip by the C_p peak and it can be considered as an artefact. Lastly, from the measured electronic and thermal transport properties, the thermoelectric figure of merit ($zT = \frac{S^2\sigma}{k}T$) was estimated as a function of temperature and it is illustrated in Fig. 5(d). The trend closely follows those of *PF* and *S*, with a minimum value of $3.4\cdot10^{-3}$ at 300 K and peaking at $4.0\cdot10^{-2}$ at 800 K.

3.3. Ab-initio calculations

Building on the VASP output files obtained in Ref. [21], transport properties were calculated using the BoltzTraP2 code between absolute zero and the Curie temperature (T_C = 426 K). In fact, calculations beyond the Curie transition are not deemed reliable. This is because, at T_C, the compound undergoes a transition from ferromagnetic to paramagnetic, causing the electronic density of states to experience significant and unpredictable shifts (DFT calculations are, by definition, performed at 0 K). The electronic band structures and density of states
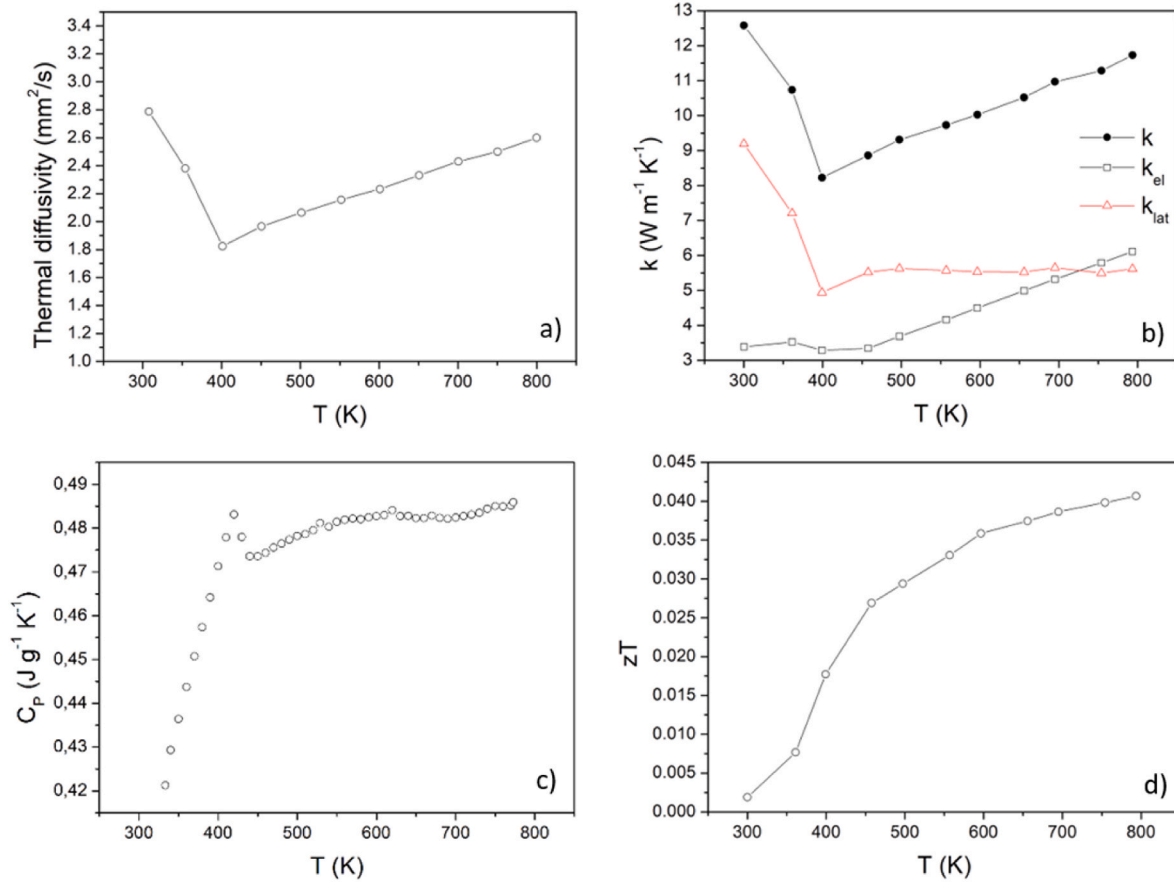
Fig. 5. Experimental values as a function of temperature of thermal diffusivity (a), thermal conductivities k (filled black circles), k_{el} (open black squares) and k_{lat} (open red triangles) (b), specific heat capacity (c) and thermoelectric figure of merit, zT, (d) for sintered Co$_2$HfSn. Lines in (a), (b) and (d) are guides to the eye.

resulting from ab-initio calculations are reported in Fig. S4 of the Supplementary Material and they do not show significant changes from those reported in Ref. [21]. A charge carrier concentration of $1.0 \cdot 10^{28}$ m^{-3}, consistent with experimental results, was chosen for the simulations.

The Seebeck coefficient dependency on T is reported in Fig. 6(a), confirming an n-type behaviour throughout the temperature range, in agreement with the experimental observations, reported in Fig. 3(a). At 300 K, a calculated value of -10.6 μV/K was obtained, which is reasonably coherent with the experimental one (-13.0 μV/K). The electrical conductivity, Fig. 6(b), and the derived electronic contribution to the thermal conductivity, Fig. 6(c), show temperature dependences similar to those observed experimentally. The figure of merit zT was also calculated, Fig. 6(d), and it turned out equal to $1.1 \cdot 10^{-6}$ at 1 K and $4.7 \cdot 10^{-3}$ at 300 K. The latter closely matches the experimental value of $3.3 \cdot 10^{-3}$. The Hall resistivity was also computed, obtaining a value of $9.2 \cdot 10^{-10}$ m^3/C at 300 K, which is close to the experimental value of $5.8 \cdot 10^{-10}$ m^3/C (see Section 3.2). The comparison between experimental and computed transport properties is limited to the temperature range between 300 K and T$_C$. On the one hand, we could not measure the transport properties (except the electrical conductivity) below room temperature and, on the other hand, we could not compute the properties above T$_C$ due to the change of the electronic structure from ferromagnetic to paramagnetic. It should be noted that the agreement between computed and experimental transport properties becomes less accurate increasing the temperature from 300 K to T$_C$. In order to explain the observed discrepancy, we should consider that the use the frozen band approximation at 0 K limits the accuracy of the computational results as the temperature approaches T$_C$. In fact, such approximation does not take in account the progressive loss of the ferromagnetic

properties that is experimentally observed just before T$_C$.

In summary, the calculated trends align well with the experimental data presented in Section 3.2 and Ref. [26]. It is worth noting that our results significantly differ from the computed values reported in Ref. [49]. However, a direct comparison is difficult, since the authors of Ref. [49] did not specify the charge carrier concentration used in their calculations, creating ambiguity in the interpretation of their results.

The computed phonon band structure and density of states (pDOS) are reported in Fig. 7(a) and (b). Given that the conventional unit cell of Co$_2$Hfsn contains 16 atoms, 48 phonon modes appear in the phonon dispersion diagram shown in Fig. 7(a). Here, the three lowest frequency modes that converge to 0 THz at the Γ point are acoustic, consisting of one longitudinal (LA), and two transverse (TA) modes. The remaining 45 optical modes, further divided into longitudinal (LO) and transverse (TO), reside at higher frequencies and stem from out-of-phase vibrations. Notably, in the low-frequency region from 0 to 2.3 THz, the acoustic branches mix with the optical branches at all high-symmetry points, except Γ. Furthermore, the two transverse acoustic modes are degenerate from the W to the L points, remaining so also from L to Γ. While a considerable overlap occurs between most of the optical-optical phonon branches, a distinct set of optical modes above 5.1 THz is separated from the rest by a minor band gap of 0.08 THz.

Considering the phonon density of states (pDOS) in Fig. 7(b), it can be observed that the low-frequency region (0–4 THz) is predominantly governed by Hf-related vibrations, as heavier atoms typically vibrate at lower frequencies. This is followed by Sn-related vibrations between 4 and 5 THz and, lastly, the modes involving Co atoms manifest as expected at high frequencies beyond 5 THz.

Several thermodynamic properties derived from the harmonic calculations, as detailed in Ref. [50], are reported in Fig. 7(c). The Helmoltz
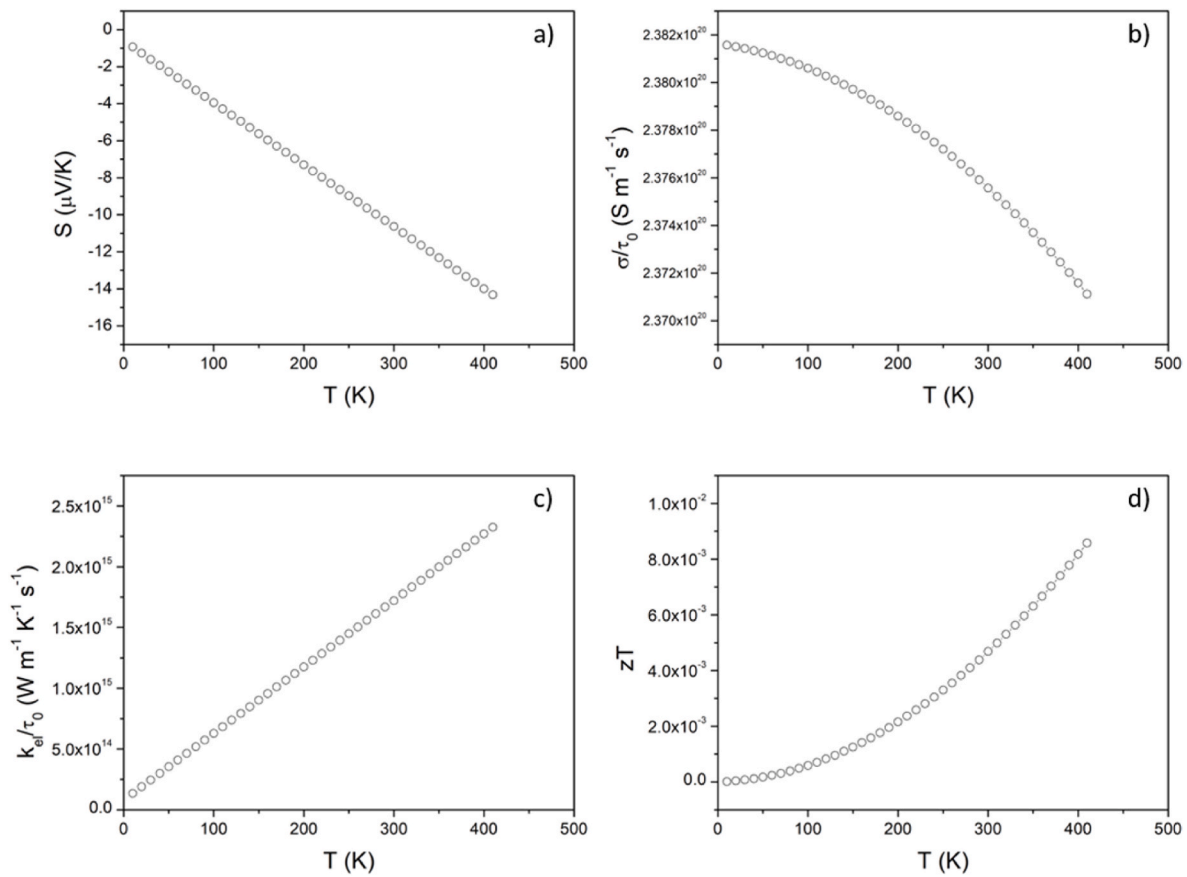
Fig. 6. Seebeck coefficient (a), electrical conductivity (b), electronic contribution to the thermal conductivity (c) and thermoelectric figure of merit, ZT, (d) of the Co_2HfSn compound calculated using the BoltzTraP2 code and considering the experimental value of the charge carrier concentration ($1.0 \cdot 10^{28}$ m^{-3}). τ_0 is the relaxation time.

free energy (red line) decreases with increasing temperature and its value at 0 K stands at 10.98 kJ/mol as atomic oscillations occur also at the absolute zero (Zero Point Energy). On the contrary, entropy (blue line), as expected, increases as a function of T and is zero at 0 K. The heat capacity at constant volume (C_v, green line) witnesses a sharp ascent with temperature up to approximately 200 K, where a plateau is reached. At low temperatures, the C_v trajectory follows approximately the Debye model, showcasing a T^3 dependence behaviour. With 4 atoms in the Co_2HfSn formula unit, the heat capacity limit should be 12 R, or 99.8 J K^{-1}mol^{-1}. When calculated beyond the Curie point to 1000 K, the C_v is 99.3 J K^{-1}mol^{-1}, in good agreement with the 12 R theoretical value and also with the previously reported 98.5 J K^{-1}mol^{-1} [49]. As shown in Fig. 5(c), an experimental value of 200.2 J K^{-1}mol^{-1} was obtained as C_p from 300 to 800 K. Considering that for incompressible substances with constant density like solids, the heat capacity at constant volume and pressure are approximately the same, there is a notable divergence between the calculated and experimental values. This discrepancy can be attributed to the harmonic approximation under which the calculations were executed. It is plausible that anharmonic effects, which exceed this approximation, are evident in the sample even at 300 K [50]. Moreover, given that this compound undergoes a ferromagnetic-paramagnetic transition, it is important to consider magnetic excitations. Such excitations often contribute significantly to the heat capacity around T_C [51] and to the entropy. However, a comprehensive assessment of these added contributions is beyond the scope of this work.

In order to estimate the lattice component of the thermal conductivity k_{lat}, a model proposed by Slack [52] has been satisfactorily used for the study of other Heusler compounds [53]. According to this model, the lattice thermal conductivity is given by

$$k_{lat} = 3.1 \cdot 10^{-6} \frac{M\theta_D\delta}{\gamma^2 n^{2/3} T} \qquad (1)$$

where θ_D is the Debye temperature in K, δ is the cubic root of the volume in Å^3, n is the number of atoms in the primitive unit cell, M is the average atomic mass in atomic unit, and γ the Grüneisen parameter. Here, θ_D and γ are calculated from the longitudinal and transverse sound velocities, which are derived from the elastic moduli (see Supplementary Material). The bulk modulus B was determined by fitting the energy-volume curve to the Murnaghan equation of state [54]:

$$E(V) = E_0(V) + \frac{BV}{B'}\left(\frac{(V_0/V)^{B'}}{B'-1}+1\right) - \frac{BV_0}{B'-1} \qquad (2)$$

where B' is the derivative of the bulk modulus, V the volume, and V_0 the volume of the fully relaxed cell. The average shear modulus was estimated by Hill [55]:

$$G = \frac{G_V + G_R}{2} \qquad (3)$$

with the G_V and G_R the Voigt [56] and Reuss [57] upper and lower bounds, respectively:

$$G_V = \frac{C_{11} - C_{12} + 3C_{44}}{5} \qquad (4)$$

$$G_R = \frac{5(C_{11} - C_{12})C_{44}}{4C_{44} + 3(C_{11} - C_{12})} \qquad (5)$$

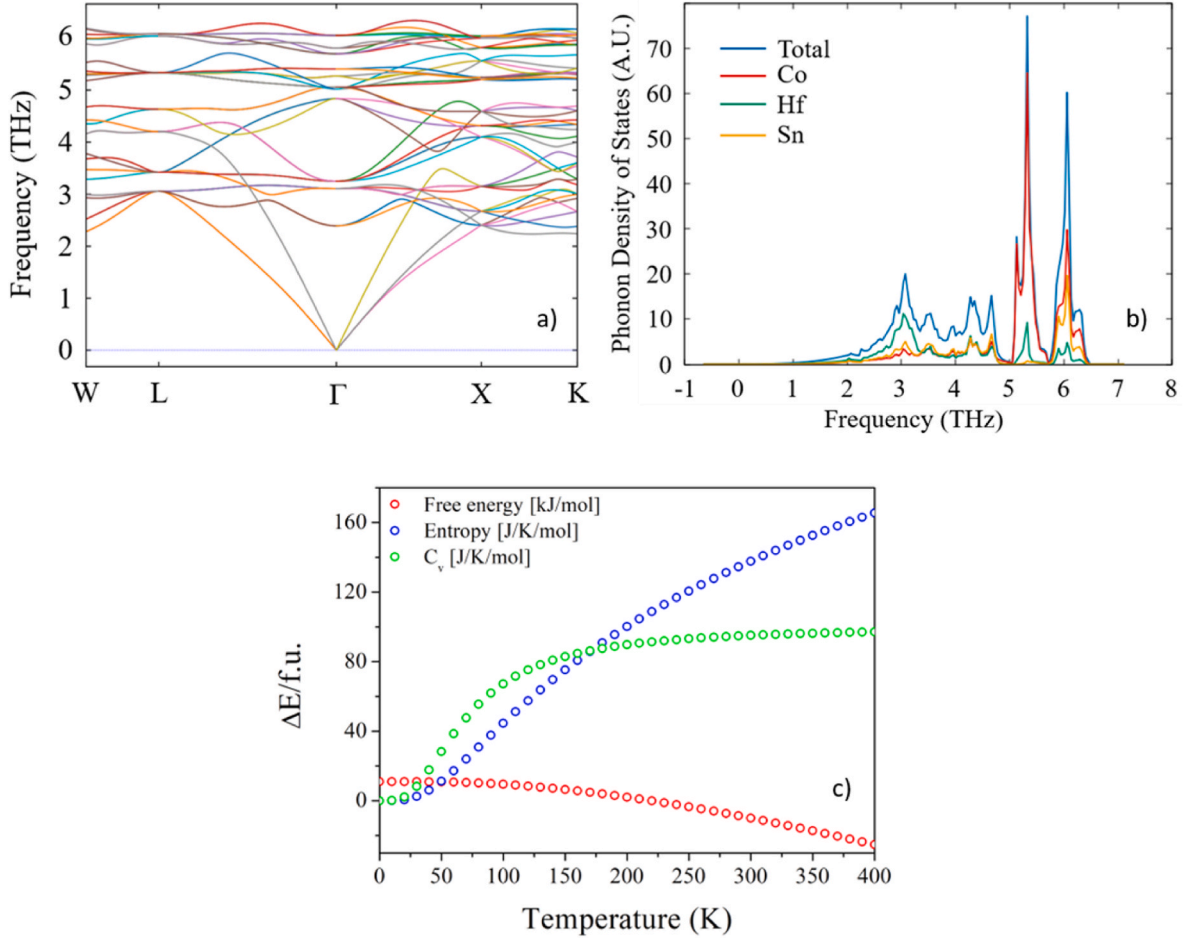This approach was adopted because there is no exact expression for

Fig. 7. (a) phonon band structure (each colour corresponds to a different vibrational mode); (b) phonon density of states; (c) thermodynamic properties of Co$_2$HfSn as a function of temperature. Each quantity is referred to moles of formula unit.

the polycrystalline average shear modulus in terms of the elastic constants C_{ij}. However, the homogenization scheme proposed in Equation (3) has been found acceptable [54]. The $C_{11} - C_{12}$ difference was obtained by applying of a volume-conserving orthorhombic strain tensor (ε) to the face centered cubic vectors:

$$\varepsilon = \begin{pmatrix} x & 0 & 0 \\ 0 & -x & 0 \\ 0 & 0 & \dfrac{x^2}{1-x^2} \end{pmatrix} \tag{6}$$

where x is the distortion parameter for a mechanically stable system, which is an even function of the total energy defined as:

$$\Delta E(x) = \Delta E(-x) = V(C_{11} - C_{12})x^2 + O[x^4] \tag{7}$$

Simultaneously, C_{44} was calculated by the application of a volume-conserving monoclinic strain tensor (ε') to the fcc vectors.

$$\varepsilon' = \begin{pmatrix} 0 & x/2 & 0 \\ x/2 & 0 & 0 \\ 0 & 0 & \dfrac{x^2}{4-x^2} \end{pmatrix} \tag{8}$$

in this case, the total energy is related to x as follows:

$$\Delta E(x) = \Delta E(-x) = \frac{1}{2} V C_{44} x^2 + O[x^4] \tag{9}$$

According to the Mehl's prescription [58], the distortion parameter x was varied between 0 and ± 0.05. Last, the Young's modulus was calculated from B and G:

$$E = \frac{9BG}{3B + G} \tag{10}$$

A summary of the elastic and thermal properties calculated for Co$_2$HfSn is shown in Table 1. Overall, all the values of the elastic constants and thermal properties are in good agreement with those already available in the literature [49].

As it can be noticed from Table 1, the calculated k_{lat} differs significantly from the experimental value reported in Fig. 5. This discrepancy arises from the assumptions underlying the Slack model. First, when the relative atomic mass difference of the elements in the alloy exceeds approximately 100 %, as in this case, k_{lat} is systematically overestimated by up to an order of magnitude. This has been previously highlighted for

Table 1

Calculated elastic constants (C), elastic moduli (B and E), Debye temperature (θ_D), Grüneisen parameter (γ), and lattice thermal conductivity at 400 K (k_{lat}) of Co$_2$HfSn.

C_{11}–C_{12} (GPa)	C_{44} (GPa)	G_V (GPa)	G_R (GPa)	G (GPa)
118	94	80	76	78
B (GPa)	**E (GPa)**	**θ_D (K)**	**γ**	**k_{lat} at 400 K (W m^{-1}K^{-1})**
161	201	361	1.72	30.8

other Heusler compounds [53]. Second, the model produces inaccurate results when the acoustic and optical phonon branches overlap, as in Co$_2$HfSn (see Fig. 7). This is due to the inability to integrate the acoustic phonon density of states separately from the optical contribution [52]. Third, this model considers only the scattering between acoustic phonons, neglecting all the other scattering phenomena, such as those with impurities, vacancies, dislocations, grain boundaries etc. [52,53]. Last, one important prescription of the Slack model is to evaluate k_{lat} at a temperature sufficiently larger than θ_D [52]. Considering that the paramagnetic transition of Co$_2$HfSn occurs at 400 K, and having the Debye temperature at 361 K, this request cannot be entirely fulfilled, being the elastic moduli calculated at 0 K in the ferromagnetic state. Setting aside this issue, the k_{lat} value at 700 K is 17.6 W m^{-1}K^{-1}, which is considerably closer to the experimental, and comparable with those reported for semiconductive Heusler compounds [53]. The problem of the overlap between acoustic and optical modes can be partially addressed according to Slack using the derivation of the Debye temperature proposed by Domb and Salter [59]. More detailed explanations on such correction are provided in the Supplementary Material; nevertheless, it was demonstrated that for face centered cubic structures, the Debye temperature can be calculated as [59]:

$$\theta'_D = \frac{h\nu_{MAX}}{k_B}\sqrt{\frac{5I(2)}{3}} = \frac{h\nu_{MAX}}{k_B}\sqrt{\frac{5}{6}} = 0.9129\frac{h\nu_{MAX}}{k_B} \tag{11}$$

where h and k_B are the Planck and Boltzmann constants, ν_{MAX} is the maximum frequency of the phonon spectrum defined in terms of force constants, and θ'_D is the newly defined Debye temperature. Being ν_{MAX} equal to 6.5 THz, see Fig. 7(b)–a θ'_D value of 285 K is obtained instead of 361 K. Substituting θ'_D in Equation (1), a k_{lat} of 15.1 W m^{-1}K^{-1} is determined at 400 K. If the electronic density of states is considered valid above T_C (as in other studies [49]), at 700 K k_{lat} is of 8.6 W m^{-1}K^{-1}. This is extremely close to the experimental value shown on Fig. 5.

4. Conclusions

The transport properties of Co$_2$HfSn Heusler compound were studied with a combination of experimental investigations and ab-initio calculations.

The alloy was synthesized by rapid solidification (melt-spinning) followed by spark-plasma sintering. This method enabled the preparation of a monophasic and stoichiometric sample with a fine microstructure and represents an advancement with respect to the multiphase sample containing off-stoichiometric Heusler compound, previously obtained in Ref. [26].

Quantitative information on the phase fractions, grain size and stoichiometry were obtained by means of several techniques such as XRD, SEM-EDS and EBSD, giving an extensive characterization of the metallurgical characteristics of samples prepared following such processing route.

Transport properties were measured from 300 K up to 800 K and, with electric conductivity measurements extending down to 2 K. Around 75 K, a change of regime of σ vs T was observed. A shift from a low-T σ/T^2 proportionality to a high-T $\sigma/T^{1.40}$ correlation occurred, which was explained in terms of different electron scattering mechanisms. In fact, as reported for other compounds [27,31], the variation of resistivity is explainable as the consequence of the presence of a half-metallic state at low temperatures (below 75 K), where the half-metallic band-gap is responsible for the hindering of spin-flip scattering. On the contrary, in the high-temperature (above 75 K) conductive state, several electron scattering mechanisms are possible, making the exponent of the σ/T dependency being comprised between 1 and 5/3 [42–44]. Coherently, an exponent value of 1.40 was experimentally observed.

The Hall resistivity was also measured from 2 to 300 K, showing anomalous properties at low fields, and ordinary behavior at higher H with relatively constant values along the whole investigated

temperature range. From the R_H data, the charge carrier concentration was estimated, resulting in values rather independent from T around $1·10^{28}$ m^{-3}, which are typical of conductive materials. Having S, σ, and k, the thermoelectric figure of merit zT was experimentally estimated here for the first time, being equal to 0.040 at its maximum value at 800 K.

Ab-initio calculations were performed on the transport properties using the BoltzTraP2 code from absolute zero to T_C. The results are in quite good agreement with experimental data at 300 K when the experimental charge carrier value concentration is chosen. The coherence between experimental results and the properties simulated for a pristine structure possibly suggests a rather ordered crystal structure in samples obtained following the chosen processing method.

The phonon band structure and density of states were also calculated, showing a vibrational behavior composed by collective motions of Co, Hf, Sn below 5 THz. Conversely, above 5 THz the phonon structure is largely dominated by modes more localized on Co-sites.

The elastic constants and bulk moduli were also calculated and used in the Slack's model framework for the estimation of the lattice thermal conductivity. Although results similar to those already reported for other Heusler compounds were obtained, several criticalities were highlighted concerning this model, which was found to systematically overestimate k_{lat} values.

The results obtained showed interesting features of the Co$_2$HfSn Heusler compound in view of potential spintronic applications, suggesting to further explore the properties of this system by deposition of thin films.

CRediT authorship contribution statement

Alessandro Difalco: Investigation, Software, Visualization, Writing – original draft. **Ignatio G. Winning:** Software. **Mauro Palumbo:** Conceptualization, Resources, Software, Writing – review & editing. **Marcello Baricco:** Resources, Writing – review & editing. **Alberto Castellero:** Conceptualization, Resources, Supervision, Writing – review & editing. **Eric Alleno:** Resources, Supervision, Writing – review & editing.

Declaration of competing interest

The authors declare that they have no known competing financial interests or personal relationships that could have appeared to influence the work reported in this paper.

Data availability

Data will be made available on request.

Acknowledgements

Appendix A. Supplementary data

Supplementary data to this article can be found online at.https://doi.org/10.1016/j.solidstatesciences.2024.107455.

References

[1] D. Beretta, N. Neophytou, J.M. Hodges, M.G. Kanatzidis, D. Narducci, M. Martin-Gonzalez, M. Beekman, B. Balke, G. Cerretti, W. Tremel, A. Zevalkink, A. I. Hofmann, C. Müller, B. Dörling, M. Campoy-Quiles, M. Caironi, Thermoelectrics: from history, a window to the future, Mater. Sci. Eng. R 138 (2019) 100501.

[2] C. Artini, G. Pennelli, P. Graziosi, Z. Li, N. Neophytou, C. Melis, L. Colombo, E. Isotta, K. Lohani, P. Scardi, et al., Roadmap on thermoelectricity, Nanotechnology 34 (2023) 292001.

[3] S.A. Khandy, I. Islam, D.C. Gupta, R. Khenata, A. Laref, Lattice dynamics, mechanical stability and electronic structure of Fe-based Heusler semiconductors, Sci. Rep. 9 (2019) 1475.

[4] V. V Khovaylo, A.I. Voronin, V.Y. Zueva, M.A. Seredina, R. Chatterdjee, Fe-based semiconducting Heusler alloys, Semiconductors 51 (2017) 718–721.

[5] E. Alleno, Review of the thermoelectric properties in nanostructured Fe$_2$VAl, Metals 8 (2018) 864.

[6] A. Diack-Rasselio, O. Rouleau, L. Coulomb, L. Georgeton, M. Beaudhuin, J.-C. Crivello, E. Alleno, Influence of self-substitution on the thermoelectric Fe$_2$VAl Heusler alloy, J. Alloys Compd. 920 (2022) 166037.

[7] S.A. Sofi, D.C. Gupta, Current research and future prospective of cobalt-based Heusler alloys as thermoelectric materials: a density functional approach, Int. J. Energy Res. 45 (2021) 4652–4668.

[8] J. Hu, S. Granville, H. Yu, Spin-dependent thermoelectric transport in cobalt-based Heusler alloys, Ann. Phys. 532 (2020) 1–20.

[9] T. Saito, D. Nishio-Hamane, Magnetic and thermoelectric properties of Co$_2$MnT (T= Ga, Si) Heusler compounds, Phys. B Condens. Matter 603 (2021) 412761.

[10] J. Barth, G.H. Fecher, B. Balke, T. Graf, A. Shkabko, A. Weidenkaff, P. Klaer, M. Kallmayer, H.-J. Elmers, H. Yoshikawa, et al., Anomalous transport properties of the half-metallic ferromagnets Co$_2$TiSi, Co$_2$TiGe and Co$_2$TiSn, Philos. Trans. R. Soc. A 369 (2011) 3588–3601.

[11] X.Y. Dong, C. Adelmann, J.Q. Xie, C.J. Palmstrøm, X. Lou, J. Strand, P.A. Crowell, J.-P. Barnes, A.K. Petford-Long, Spin injection from the Heusler alloy Co$_2$MnGe into Al$_{0.1}$Ga$_{0.9}$As/GaAs heterostructures, Appl. Phys. Lett. 86 (2005) 102107.

[12] A. Hirohata, D.C. Lloyd, Heusler alloys for metal spintronics, MRS Bull. 47 (2022) 593–599.

[13] K. Inomata, N. Ikeda, N. Tezuka, R. Goto, S. Sugimoto, M. Wojcik, E. Jedryka, Highly spin-polarized materials and devices for spintronics, Sci. Technol. Adv. Mater. 9 (2008) 14101.

[14] N.I. Kourov, A. V Korolev, V. V Marchenkov, A V Lukoyanov, K.A. Belozerova, Magnetic and electrical properties of the half-metallic ferromagnets Co$_2$CrAl, Phys. Solid State 55 (2013) 977–985.

[15] L. Ritchie, G. Xiao, Y. Ji, T.Y. Chen, C.L. Chien, M. Zhang, J. Chen, Z. Liu, G. Wu, X. X. Zhang, Magnetic, structural, and transport properties of the Heusler alloys Co$_2$MnSi and NiMnSb, Phys. Rev. B 68 (2003) 104430.

[16] S. Wurmehl, G.H. Fecher, H.C. Kandpal, V. Ksenofontov, C. Felser, H.-J. Lin, J. Morais, Geometric, electronic, and magnetic structure of Co$_2$FeSi: Curie temperature and magnetic moment measurements and calculations, Phys. Rev. B 72 (2005) 184434.

[17] T. Kanomata, Y. Chieda, K. Endo, H. Okada, M. Nagasako, K. Kobayashi, R. Kainuma, R.Y. Umetsu, H. Takahashi, Y. Furutani, et al., Magnetic properties of the half-metallic Heusler alloys Co$_2$VAl and Co$_2$VGa under pressure, Phys. Rev. B 82 (2010) 144415.

[18] J. Kübler, G.H. Fecher, C. Felser, Understanding the trend in the Curie temperatures of Co$_2$-based Heusler compounds: ab initio calculations, Phys. Rev. B 76 (2007) 24414.

[19] R. Shan, H. Sukegawa, W.H. Wang, M. Kodzuka, T. Furubayashi, T. Ohkubo, S. Mitani, K. Inomata, K. Hono, Demonstration of half-metallicity in fermi-level-tuned Heusler alloy Co$_2$FeAl$_{0.5}$Si$_{0.5}$ at room temperature, Phys. Rev. Lett. 102 (2009) 246601.

[20] T. Kanomata, Y. Amako, Y. Ida, Y. Adachi, T. Osaki, T. Eto, H. Nishihara, I. Shigeta, S. Imada, M. Doi, Magnetic properties of ferromagnetic Heusler alloy Co$_2$ZrSn, J. Phys. Chem. Solid. 164 (2022) 110635.

[21] A. Difalco, G. Barrera, M. Palumbo, A. Castellero, M. Baricco, P.M. Tiberto, P. Allia, Itinerant magnetism, electronic properties and half-metallicity of Co$_2$ZrSn and Co$_2$HfSn Heusler alloys, J. Alloys Compd. 918 (2022) 165464.

[22] A. Rahman, M.U. Rehman, H. Zhao, W. Liu, J. Wang, Y. Lu, K. Ruan, R. Dai, Z. Wang, X. Tao, others, Itinerant magnetism in the half-metallic Heusler compound Co$_2$HfSn: evidence from critical behavior combined with first-principles calculations, Phys. Rev. B 103 (2021) 94425.

[23] S.A. Wolf, D.D. Awschalom, R.A. Buhrman, J.M. Daughton, von S. von Molnár, M. L. Roukes, A.Y. Chtchelkanova, D.M. Treger, Spintronics: a spin-based electronics vision for the future, Science 294 (2001) 1488–1495.

[24] I. Žutić, J. Fabian, S. Das Sarma, Spintronics: fundamentals and applications, Rev. Mod. Phys. 76 (2004) 323.

[25] K. Uchida, S. Takahashi, K. Harii, J. Ieda, W. Koshibae, K. Ando, S. Maekawa, E. Saitoh, Observation of the spin Seebeck effect, Nature 455 (2008) 778–781.

[26] A. Difalco, F. Aversano, S. Boldrini, A. Ferrario, M. Baricco, A. Castellero, Synthesis and characterization of thermoelectric Co$_2$XSn (X = Zr, Hf) Heusler alloys, Metals 10 (2020) 624.

[27] P. Turban, S. Andrieu, B. Kierren, E. Snoeck, C. Teodorescu, A. Traverse, Growth and characterization of single crystalline NiMnSb thin films and epitaxial NiMnSb/MgO/NiMnSb (001) trilayers, Phys. Rev. B 65 (2002) 134417.

[28] H.S. Cherif, A. Bentouaf, Z.A. Bouyakoub, H. Rached, B. Aïssa, Computational determination of structural, electronic, magnetic and thermodynamic properties of Co$_2$HfZ (Z= Al, Ga, Si and Sn) full Heusler compounds for spintronic applications, J. Alloys Compd. 894 (2022) 162503.

[29] S. Babiker, G. Gao, K. Yao, Half-metallicity and magnetism of Heusler alloys Co$_2$HfZ (Z= Al, Ga, Ge, Sn), J. Magn. Magn Mater. 441 (2017) 356–360.

[30] M. Yin, S. Chen, P. Nash, Enthalpies of formation of selected Co$_2$YZ Heusler compounds, J. Alloys Compd. 577 (2013) 49–56.

[31] C. Hordequin, D. Ristoiu, L. Ranno, J. Pierre, On the cross-over from half-metal to normal ferromagnet in NiMnSb, Eur. Phys. J. B 16 (2000) 287–293.

[32] MAUD, Materials Analysis Using Diffraction, 2023. https://luttero.github.io/maud/. (Accessed 15 March 2023).

[33] O. Rouleau, E. Alleno, Measurement system of the Seebeck coefficient or of the electrical resistivity at high temperature, Rev. Sci. Instrum. 84 (2013) 105103.

[34] G. Kresse, J. Furthmüller, Efficient iterative schemes for ab initio total-energy calculations using a plane-wave basis set, Phys. Rev. B 54 (1996) 11169.

[35] P.E. Blöchl, Projector augmented-wave method, Phys. Rev. B 50 (1994) 17953.

[36] G.K.H. Madsen, J. Carrete, M.J. Verstraete, BoltzTraP2, a program for interpolating band structures and calculating semi-classical transport coefficients, Comput. Phys. Commun. 231 (2018) 140–145.

[37] G. Kresse, D. Joubert, From ultrasoft pseudopotentials to the projector augmented-wave method, Phys. Rev. B 59 (1999) 1758.

[38] J.P. Perdew, K. Burke, M. Ernzerhof, Generalized gradient approximation made simple, Phys. Rev. Lett. 77 (1996) 3865–3868.

[39] H.J. Monkhorst, J.D. Pack, Special points for Brillouin-zone integrations, Phys. Rev. B 13 (1976) 5188.

[40] A. Togo, First-principles phonon calculations with phonopy and phono3py, J. Phys. Soc. Japan. 92 (2023) 12001.

[41] K.R.A. Ziebeck, P.J. Webster, A neutron diffraction and magnetization study of Heusler alloys containing Co and Zr, Hf, V or Nb, J. Phys. Chem. Solid. 35 (1974) 1–7.

[42] M.J. Otto, H. Feil, R.A.M. Van Woerden, J. Wijngaard, P.J. Van Der Valk, C.F. Van Bruggen, C. Haas, Electronic structure and magnetic, electrical and optical properties of ferromagnetic Heusler alloys, J. Magn. Magn Mater. 70 (1987) 33–38.

[43] J. Pierre, R. V Skolozdra, J. Tobola, S. Kaprzyk, C. Hordequin, M.A. Kouacou, I. Karla, R. Currat, E. Lelievre-Berna, Properties on request in semi-Heusler phases, J. Alloys Compd. 262 (1997) 101–107.

[44] K. Ueda, T. Moriya, Contribution of spin fluctuations to the electrical and thermal resistivities of weakly and nearly ferromagnetic metals, J. Phys. Soc. Japan. 39 (1975) 605–615.

[45] D. Ristoiu, J.P. Nozieres, L. Ranno, Epitaxial NiMnSb thin films prepared by facing targets sputtering, J. Magn. Magn Mater. 219 (2000) 97–103.

[46] H.-S. Kim, Z.M. Gibbs, Y. Tang, H. Wang, G.J. Snyder, Characterization of Lorenz number with Seebeck coefficient measurement, Apl. Mater. 3 (2015) 041506.

[47] F. Völklein, H. Reith, T.W. Cornelius, M. Rauber, R. Neumann, The experimental investigation of thermal conductivity and the Wiedemann-Franz law for single metallic nanowires, Nanotechnology 20 (2009) 325706.

[48] X. Xu, M. Nagasako, M. Kataoka, R.Y. Umetsu, T. Omori, T. Kanomata, R. Kainuma, Anomalous physical properties of Heusler-type Co$_2$Cr (Ga, Si) alloys and thermodynamic study on reentrant martensitic transformation, Phys. Rev. B 91 (2015) 104434.

[49] M.Y. Raiâ, R. Masrour, M. Hamedoun, J. Kharbach, A. Rezzouk, A. Hourmatallah, N. Benzakour, K. Bouslykhane, Stability, magnetic, electronic, elastic, thermodynamic, optical, and thermoelectric properties of Co$_2$TiSn, Co$_2$ZrSn and Co$_2$HfSn Heusler alloys from calculations using generalized gradient approximation techniques, J. Mater. Sci. Mater. Electron. 33 (2022) 20229–20256.

[50] M. Palumbo, B. Burton, A. e Silva, B. Fultz, B. Grabowski, G. Grimvall, B. Hallstedt, O. Hellman, B. Lindahl, A. Schneider, et al., Thermodynamic modelling of crystalline unary phases, Phys. Status Solidi 251 (2014) 14–32.

[51] F. Körmann, A.A.H. Breidi, S.L. Dudarev, N. Dupin, G. Ghosh, T. Hickel, P. Korzhavyi, J.A. Munoz, I. Ohnuma, Lambda transitions in materials science: recent advances in CALPHAD and first-principles modelling, Phys. Status Solidi 251 (2014) 53–80.

[52] G.A. Slack, The thermal conductivity of nonmetallic crystals, Solid State Phys. 34 (1979) 1–71.

[53] C. Barreteau, J.-C. Crivello, J.-M. Joubert, E. Alleno, Optimization of criteria for an efficient screening of new thermoelectric compounds: the TiNiSi structure-type as a case-study, ACS Comb. Sci. 22 (2020) 813–820.

[54] A. Breidi, S.G. Fries, M. Palumbo, A. V Ruban, First-principles modeling of energetic and mechanical properties of Ni-Cr, Ni-Re and Cr-Re random alloys, Comput. Mater. Sci. 117 (2016) 45–53.

[55] R. Hill, The elastic behaviour of a crystalline aggregate, Proc. Phys. Soc. 65 (1952) 349.

[56] W. Voigt, et al., On the relation between the elasticity constants of isotropic bodies, Ann. Phys. Chem. 274 (1889) 573–587.

[57] A. Reuss, Berechnung der Fliessgrenze von Mischkristallen auf Grund der Plastizitätsbedingung für Einkristalle, ZAMM J. Appl. Math. Mech. 9 (1929) 49–58.

[58] M.J. Mehl, Pressure dependence of the elastic moduli in aluminum-rich Al-Li compounds, Phys. Rev. B 47 (1993) 2493.

[59] C. Domb, L. Salter, CIX, The zero point energy and Θ crystals, London, Edinburgh, Dublin Philos. Mag. J. Sci. 43 (1952) 1083–1089.